ELSEVIER

Contents lists available at ScienceDirect

Measurement

journal homepage: www.elsevier.com/locate/measurement



A new approach for damage detection in asphalt concrete pavements using battery-free wireless sensors with non-constant injection rates



Hassene Hasni ^{a,*}, Amir H. Alavi ^a, Pengcheng Jiao ^a, Nizar Lajnef ^a, Karim Chatti ^a, Kenji Aono ^b, Shantanu Chakrabartty ^b

ARTICLE INFO

Article history:
Received 3 November 2016
Received in revised form 22 June 2017
Accepted 27 June 2017
Available online 28 June 2017

Keywords: Self-powered wireless sensor Non-constant injection rate Finite element modeling Polyvinylidene fluoride Damage detection

ABSTRACT

This study presents a novel approach for detection of bottom-up cracking in asphalt concrete (AC) pavements using self-powered wireless sensor (SWS) with non-constant injection rates. The performance of the sensors was evaluated through numerical and experimental studies on an asphalt concrete specimen under three-point bending configuration. Damage was introduced by making notches with different sizes at the bottom of the specimen. Different 3D finite element (FE) models were developed using ABAQUS to generate the sensor output data for different damage states. Thereafter, the laboratory tests were carried on the same specimen to validate the performance of the proposed damage detection approach. Polyvinylidene fluoride (PVDF) piezoelectric film was used to harvest the strain energy from the host structure and empower the sensor. In order to protect the embedded sensor, an H-shape packaging system was designed and tested. The results indicate that the progression of bottom-up cracks can be accurately detected using the proposed self-powered sensing system.

© 2017 Elsevier Ltd. All rights reserved.

1. Introduction

Continuous condition monitoring is an essential factor to enhance the safe operation and in-service performance of pavement systems. In this context, the existing health monitoring methods can generally be categorized into two groups: the insitu pavement sensors and external evaluation technologies [1]. During the past two decades, the in-situ sensing techniques have been developed as the alternatives to the traditional monitoring methods [2-5]. Many types of sensors are used in this method such as deflectometer, fiber-optic sensors, moisture sensor, pressure cell, strain gauge, thermocouple, accelerometers, etc. [2-10]. The external evaluation approaches are extensively used to detect surface distresses of pavement, i.e., pavement distresses evaluation based on image analysis [11–12], or pavement deformation detection by stereo-imagery [13-18]. Deployment and maintenance of such wired systems is a challenging task. The other issue is to effectively manage massive data created by the wired sensors [19]. In order to overcome such limitations, wireless sensor networks (WSNs) have been widely used in the area of structural health monitoring (SHM) [20-23]. However, finding a costeffective and sustainable power source is one of the obstacles for wide application of wireless sensors. Harvesting ambient energy has been proved to be a viable solution for this problem [24-34]. Among different energy harvesting resources, piezoelectric transducers are one of the most efficient options [28-30,35]. Recently, our research group at Michigan State University (MSU) has developed a new type of piezo-based self-powered wireless sensor (SWS) [35-38]. A porotype of the SWS is shown in Fig. 1. This sensor is based on the integration of a piezoelectric transducer with an array of ultra-low power floating gate computational circuit [35]. By embedding the SWS inside the pavement system, the localized strain statistics can be continuously monitored. The information recorded on-board the sensor can be read using radio frequency (RF) technology. The SWSs have floatinggates with constant injection and non-constant injection rates. The main difference between the two classes of SWS is in the form of data outputted from the sensors. There are very few studies on the applicability of the SWS with constant injection rates for SHM [35,37-40]. In a recent study, Alavi et al. [38] have tested the ability of the sensor for detection and localizing bottom-up cracking in asphalt pavement using the SWS with constant injection rate. They have characterized the sensor output using a cumulative density function (CDF) and defined new damage

^a Department of Civil and Environmental Engineering, Michigan State University, East Lansing, MI 48824, USA

^b Department of Computer Science & Engineering, Washington University, Saint Louis, MO 63130, USA

^{*} Corresponding author.

E-mail addresses: hasniha1@msu.edu (H. Hasni), ah_alavi@hotmail.com, alavi@msu.edu (A.H. Alavi).

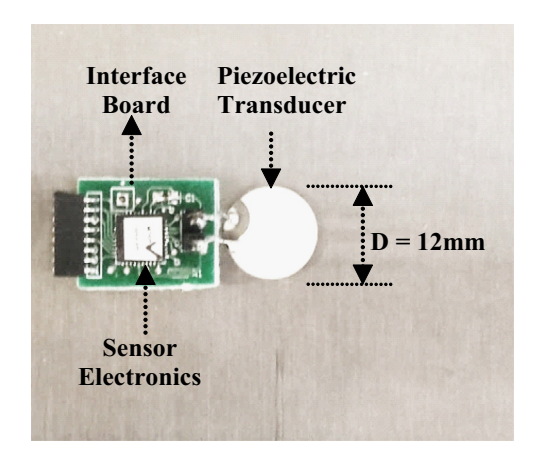


Fig. 1. Prototype of the self-powered wireless sensing system.

indicators. The CDF parameters were found to be good damage predictors.

However, the variability of the injection rate in the floating gates results in a notable difficulty in the interpretation of the SWS data compared to a constant injection rate type of sensors. In fact, for the case of non-constant injection rates, the sensor data cannot be characterized with a CDF and require a new data analysis framework. In this paper, the applicability of a new health monitoring system for pavements using SWS with non-constant injection rates is investigated for the detection of bottom-up pavement cracking. The numerical and experimental studies were focused on the detection of progression of bottom-up cracking caused by excessive strains at the bottom of an asphalt-concrete specimen. The results indicate that the proposed approach has a satisfactory performance for the detection of damage progression in pavement structures.

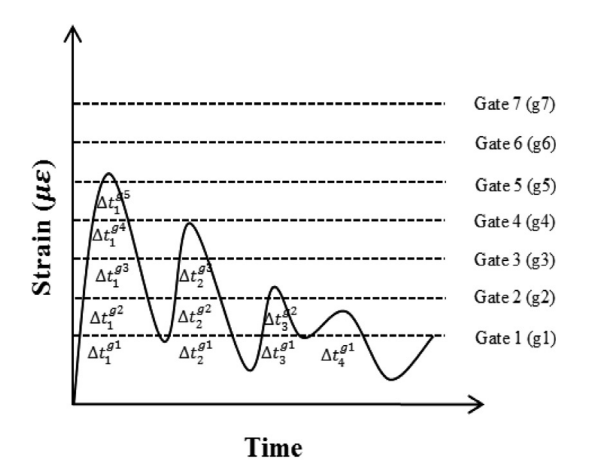
2. Working principle of non-constant injection rate SWS

The new developed sensor at MSU has seven memory cells that monitor the cumulative strain events induced by mechanical loading. The sensing mechanism includes two main phases: harvesting the energy from the structure under loading using a piezoelectric transducer, and recording the cumulative voltage (respectively strain) events via the sensor electronics. Piezoelectric transducers are used to transform mechanical loads into electrical charges. The open source voltage (V) across a piezoelectric transducer is given by:

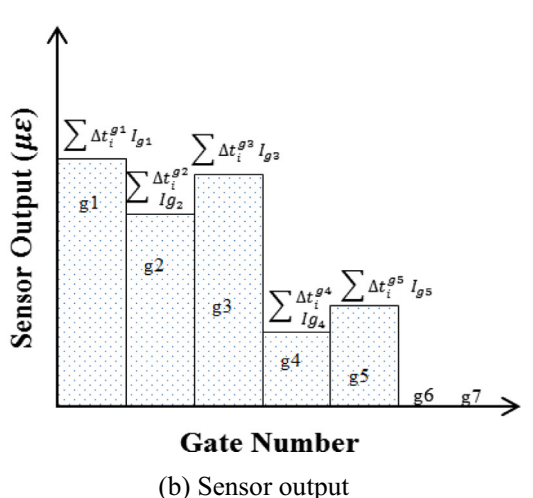
$$V = \frac{SY \, d_{31} \, h}{\varepsilon} \tag{1}$$

where S, Y, d_{31} , h and ε are the applied strain, Young's modulus (Pa) of the piezoelectric material, piezoelectric constant (C/N), thickness (m), and electrical permittivity (F/m), respectively. The piezoelectric transducers can be attached anywhere in the structure to harvest the strain energy and convert it into an electric charge. The resulting electrical energy is then used to empower the sensor as well as to monitor the health status of the structure. The sensor unit including the floating gates is connected to the piezoelectric transducer to record the data. Each gate (cell) has a specific threshold level and injection rate. When the amplitude of the strain at the sensor location exceeds the threshold level of a specific gate, it starts recording the cumulative strain droppage. The injection rate is defined as the quantity of droppage in strains during 1 s at a specific memory gate.

Fig. 2 displays the procedure of obtaining the strain droppage $(\varepsilon_0 - \varepsilon_{sensor})$ at the sensor level. As seen in this figure, the sensor strain droppage is in the form of a histogram that has different



(a) Strain versus time



(b) Sensor output

Fig. 2. Cumulative loading time estimation by the SWS.

amplitudes for each gate. In fact, each memory cell has an initial strain value ε_0 . After applying a certain number of loading cycles, the initial strain decreases linearly with the number of cycles. In Fig. 2(a), the resulting cumulative time intersections at gate gi is given as:

$$\Delta t_i = \sum_i \Delta t_k^{gi} \tag{2}$$

Furthermore, the strain value ε_{sensor} at each gate can be written as:

$$\varepsilon_{\text{sensor}} = \varepsilon_0 - I_{g_i} \Delta t_i \tag{3}$$

where I_{g_i} is the strain injection rate defined in $\mu\epsilon/s$ and Δt_k^{gi} is the k^{th} time intersection interval at gate g_i . In this paper, the case of a non-constant injection rate sensor was studied. Thus, the shape of the histogram does not follow a specific trend. The injection rates play a very important role in defining the sensor output. Note that the strain and voltage variations are proportional according to Eq. (1) and therefore, the strain droppage or voltage droppage $(V_0 - V_{sensor})$ can be used in the proposed relative damage approach.

The strain injection rate parameter is a property of the sensor that controls the speed of variation of the sensor strain as a function of time. Alavi et al. [37] showed that the output histogram of a constant injection rate sensor can be characterized by a Gaussian distribution. For the sensors used in this study, the shape of

the output histogram is different and fully controlled by the injection rates. Therefore, a new approach was proposed to define new damage indicator features and detect damage progression in asphalt concrete (AC) pavements.

The analysis carried out in this study was divided into two stages. First, a finite element (FE) model was developed to obtain the structural response of the beam under different damage scenarios. The strains were extracted at the sensing node and then a MATLAB script was developed to obtain the cumulative loading time for each gate and for each damage state. The sensor output was calculated using Eq. (3). Thereafter, the percentage of strain droppage for different damage states was estimated based on the sensor output data. For the second step, the voltage droppage and the percentage of voltage droppage were directly calculated using the measured sensor data. Fig. 3 shows a flowchart of the proposed method.

3. Numerical study

3.1. Description of the FE model

The performance of the sensor was numerically investigated through the simulation of an asphalt concrete specimen. The

sample was modeled under three-point bending mode. The loading protocol included applying a gradually increasing compressive force to the top mid-span of the beam. A schematic illustration of the test is shown in Fig. 4.

Damage was introduced by making a notch at the middle of the bottom of the asphalt concrete specimen. The damage states were defined by increasing the notch size (a) as follows:

- Intact (D0): *a* = 0 mm
- Damage 1 (D1): *a* = 6.35 mm
- Damage 2 (D2): *a* = 15.87 mm
- Damage 3 (D3): *a* = 19.10 mm
- Damage 4 (D4): *a* = 25.30 mm

For the analysis, the initial strain value of each channel was set to ε_0 = 300 $\mu\varepsilon$. The gate injection rates as well as the strain threshold levels are displayed in Table 1.

The selection of the thresholds and injection rates was based on an existing sensor and piezoelectric transducer. In fact, each of the sensor gates has specific voltage threshold level from which the gate starts recording the data. Therefore, depending on the type of the piezoelectric transducer, the strain thresholds can be determined experimentally by gradually increasing the applied strain to

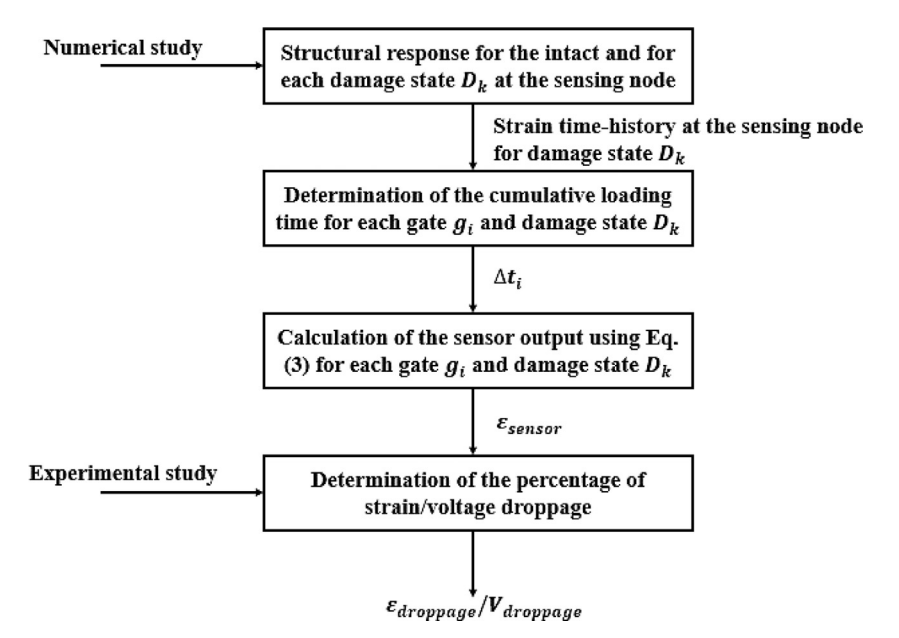


Fig. 3. Flowchart of the proposed method.

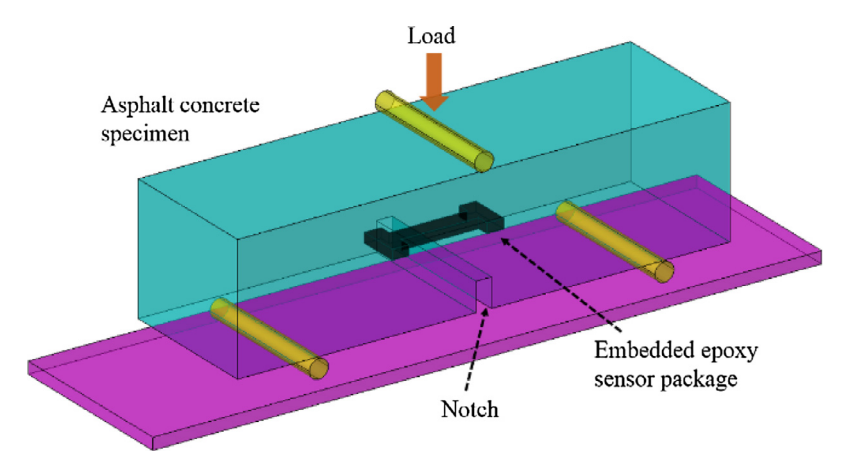


Fig. 4. Schematic of the notched asphalt concrete specimen under three-point bending test.

Table 1The preselected strain levels and the gate injection rates considered for the analysis.

| Gate number | Strain threshold level $(\mu\varepsilon)$ | Injection rate $(\mu \varepsilon/\mathbf{s})$ |
|-------------|---|---|
| 1 | 300 | 9.5 |
| 2 | 400 | 17.11 |
| 3 | 500 | 9 |
| 4 | 600 | 22.5 |
| 5 | 700 | 20.4 |
| 6 | 800 | 30.4 |
| 7 | 900 | 14.2 |

the piezoelectric transducer and recording the corresponding drop in voltage for each gate of the sensor.

The activation strain of the sensor is 300 $\mu\epsilon$ below which the device does not record any information. The maximum threshold is 900 $\mu\epsilon$ where all the channels are activated. Different 3D FE

Table 2 Constant values, a_i , used in the analysis.

| a_1 | a_2 | a_3 | a_4 |
|-------|-------|-------|--------|
| 0.639 | 3.341 | 0.709 | -0.691 |

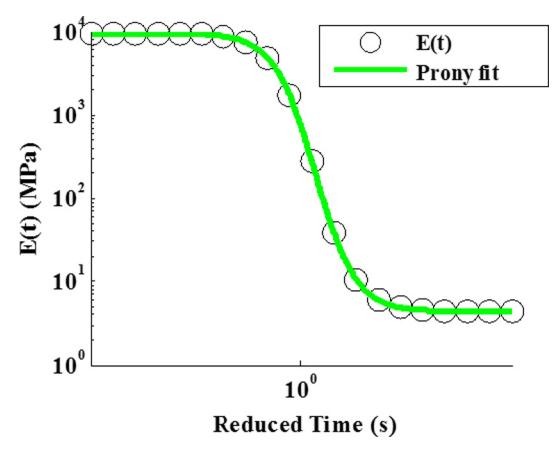


Fig. 5. Fitted relaxation modulus to Prony series representation.

models were developed for each damage state to analyze the dynamic response of the asphalt concrete beam under a dynamic loading. ABAQUS/CAE 6.11 was used for the modeling and post-processing of the results. Dynamic implicit procedure was selected for the analysis. A displacement of 0.5 mm was applied to the upper part of the beam. The applied load has the following shape:

$$u_{applied} = \frac{A}{2} [1 - \cos(2\pi f t)] \tag{4}$$

where f(f = 2 Hz) is the frequency and A(A = 0.5 mm) is the amplitude of the applied displacement.

The sample was modeled using a viscoelastic material. The relaxation modulus of the asphalt concrete material used in this paper was defined by four constants $a_i (i=1,2,3,4)$ as follows:

$$Log(E(t)) = a_1 + \frac{a_2}{1 + e^{-a_3 - a_4 \log(t_r)}} \tag{5}$$

where t_r is the reduced time, and a_i are coefficients related to the type of the AC material. The constants a_i used in this study are summarized in Table 2. Eq. (5) was fitted to the Prony representation of the asphalt concrete modulus given by:

$$E(t) = E_0 - \sum_{i=1}^{n} E_i \left(1 - e^{-\frac{t}{\tau_i}} \right)$$
 (6)

where E_0 represents the instantaneous modulus and (E_i, τ_i) are the Prony series parameters. The Prony series parameters should be given as normalized quantities in ABAQUS: The dimensionless shear relaxation modulus \bar{g}_i , the dimensionless bulk relaxation modulus \bar{k}_i , and the relaxation time τ_i . The shear (G) and bulk (K) moduli are given as:

$$\begin{cases} G(t) = \frac{E(t)}{2(1+\nu)} \\ K(t) = \frac{E(t)}{3(1-2\nu)} \end{cases}$$
 (7)

Fig. 5 shows the fitted relaxation modulus from Eq. (5) to the Prony representation given by Eq. (6). The viscoelastic properties used in the FE model are summarized in Appendix A. The instantaneous modulus E_0 is 9548 MPa.

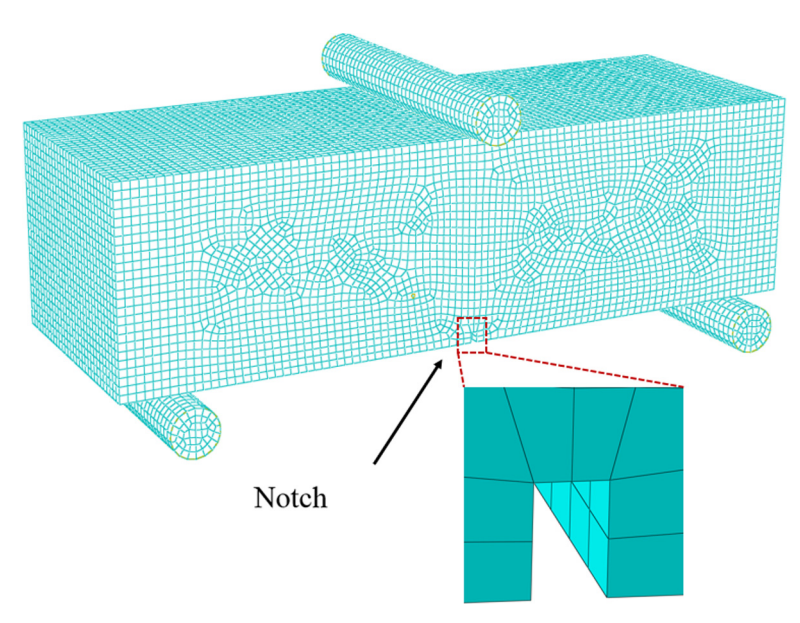


Fig. 6. FE model mesh.

3.2. FE simulations results

The asphalt concrete beam was modeled using 9615 linear hexahedral elements of type (C3D8R). Mesh refining technique was adopted for the meshing strategy in order to capture high stresses and strains concentration around the crack tip. The obtained optimal element size was about 10 mm for the intact configuration. The entire length of the slab was equal to 450 mm (17.71 in), the span length is 381 mm (15 in), the thickness is 127 mm (5 in), and the width is 152.4 mm (6 in). The rollers have a diameter of 30 mm (1.18 in) and are setup to be free in rotation. The point of measurement was located at a distance of 30 mm from the middle bottom of the specimen. The meshed model of the beam is shown in Fig. 6. Fig. 7 displays the results of the longitudinal strains (along the slab length) for the five damage states (D0, D1, D2, D3, D4). As one would expect, the amplitude of the strain increases as the damage progresses. This is mainly due to the stress concentration around the notch tip. Fig. 8 displays the sensor output histogram

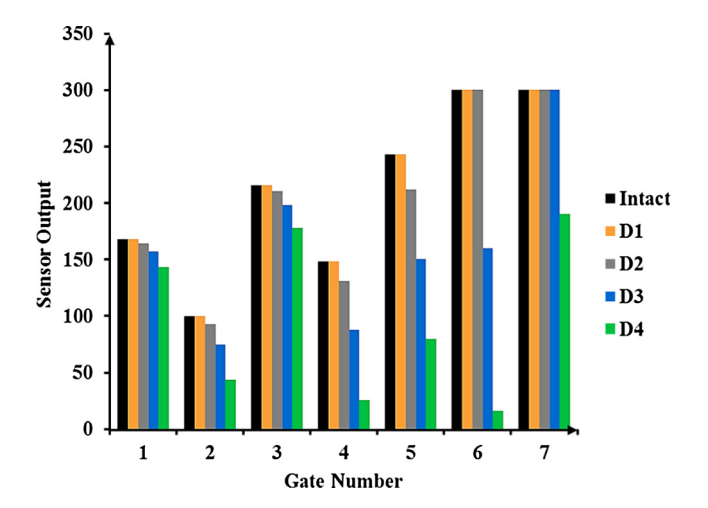


Fig. 8. Histograms representing the output of the sensor with non-constant injection rate.

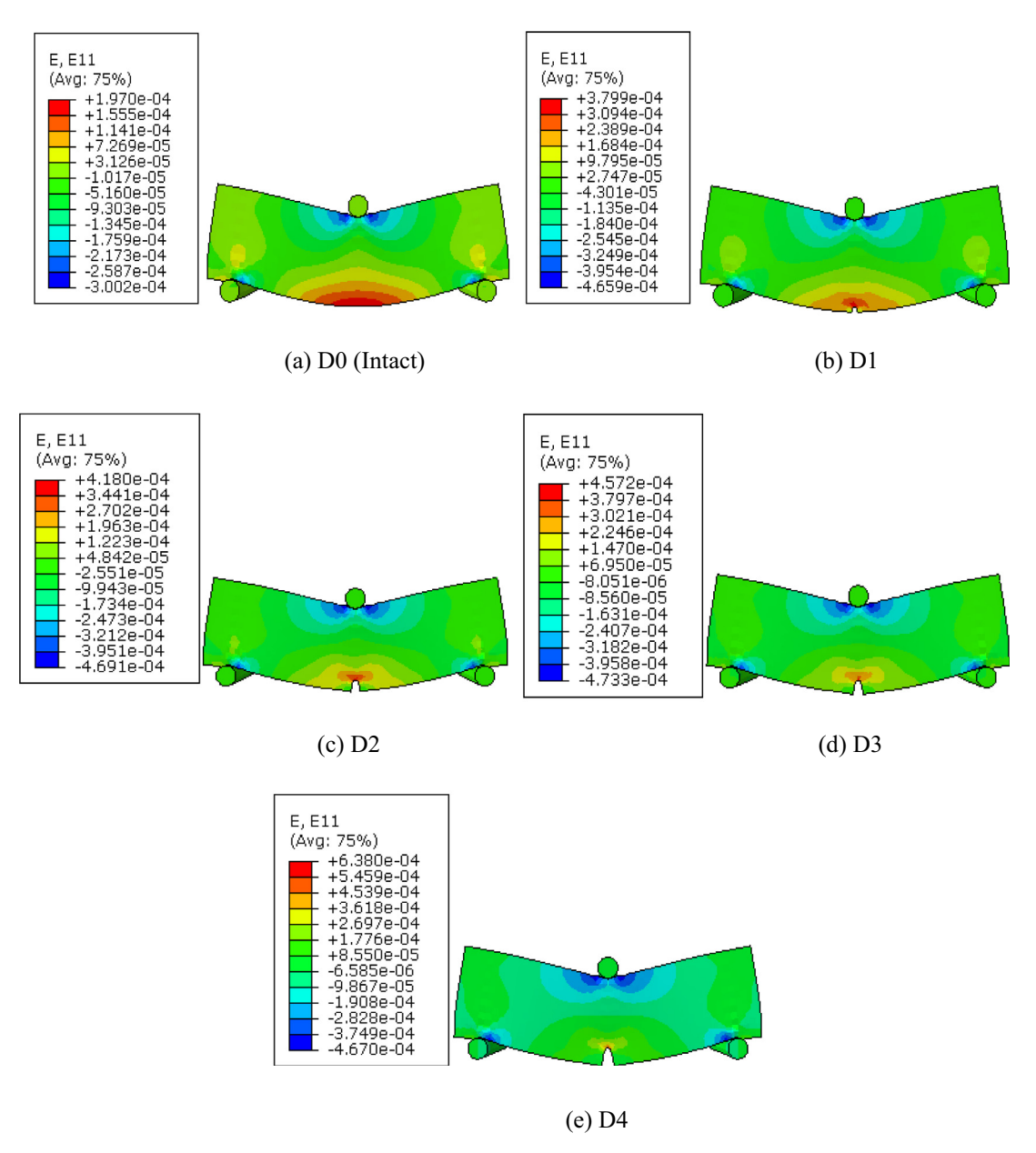


Fig. 7. FE simulation results.

for each damage state. It can be seen that the sensor strain shows a decreasing trend between damage states for all of the sensor channels. However, some channels do not record any change in the

strain values between damage states. In particular, the outputs for $\{D0, D1, D2\}$ of gate 6, and $\{D0, D1, D2, D3\}$ of gate 7 are the same.

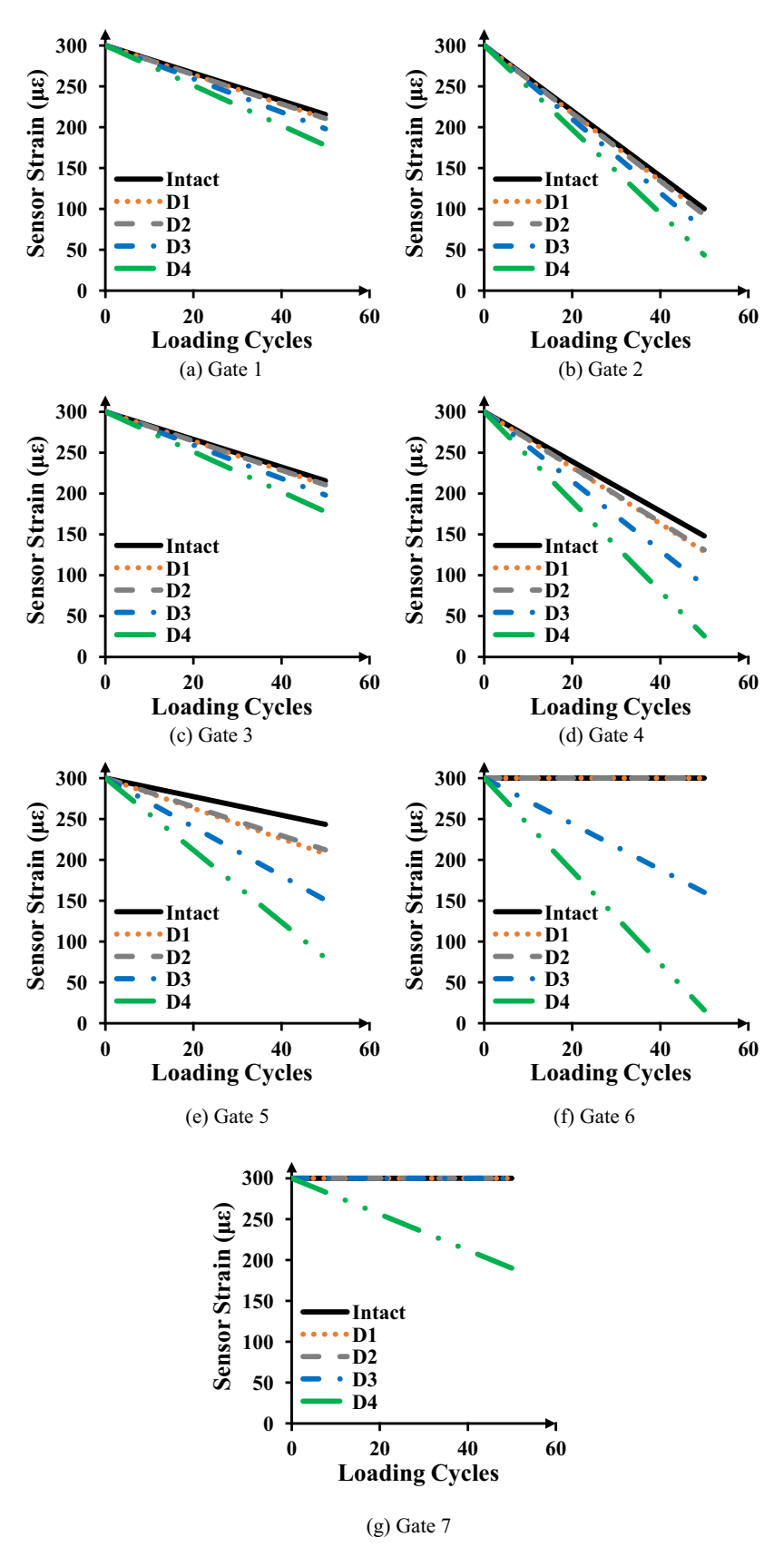


Fig. 9. Strain changes across the floating-gates of the SWS.

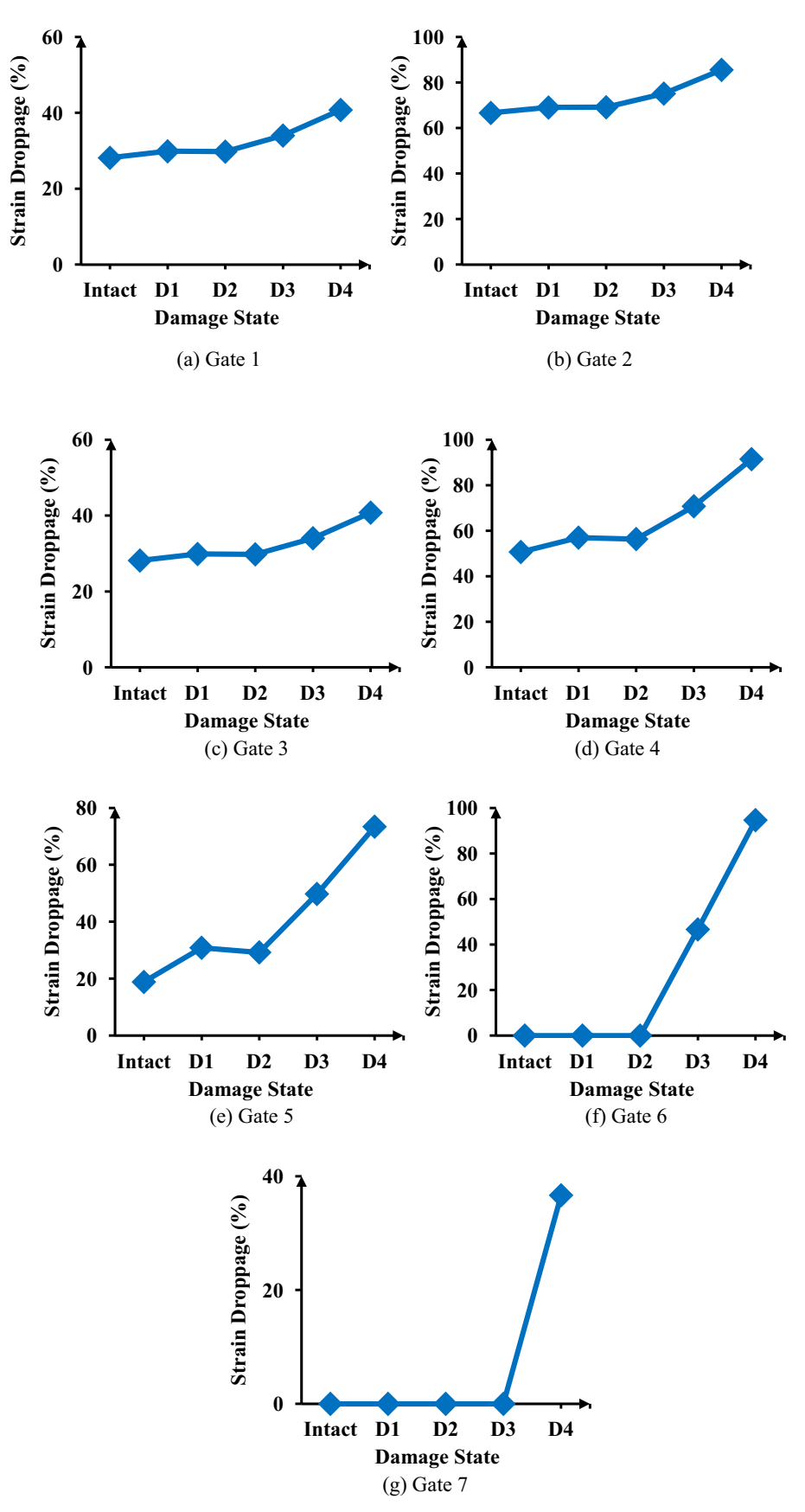


Fig. 10. Percentage of strain droppage for different gates of the sensor.

3.3. Damage detection results

Fig. 9 presents the variation of the sensor strain at each gate against the number of applied cycles for each damage state. Fig. 10. displays the percentage of the sensor strain droppage after 50 cycles. As seen, the strain varies linearly with the number of cycles. Furthermore, the intact configuration has the smallest slope (in absolute value) compared to other damage states. The percentage of voltage droppage notably increases due to the damage

progression. In fact, when the notch size increases, the longitudinal strain (along the slab length) increases as well. Thus, the cumulative time durations $\Delta t_i (i=1..7)$ measured by each gate increases. As seen in Fig. 9, the recorded strain droppage of the sensor highly depends on the damage state. When the strain exceeds a threshold corresponding to one of the gates, the sensor strain starts decreasing. Conversely, if the strain value is below the gate injection threshold, the sensor strain does not change. As an example, the strain amplitude for all damage states is higher than the activation

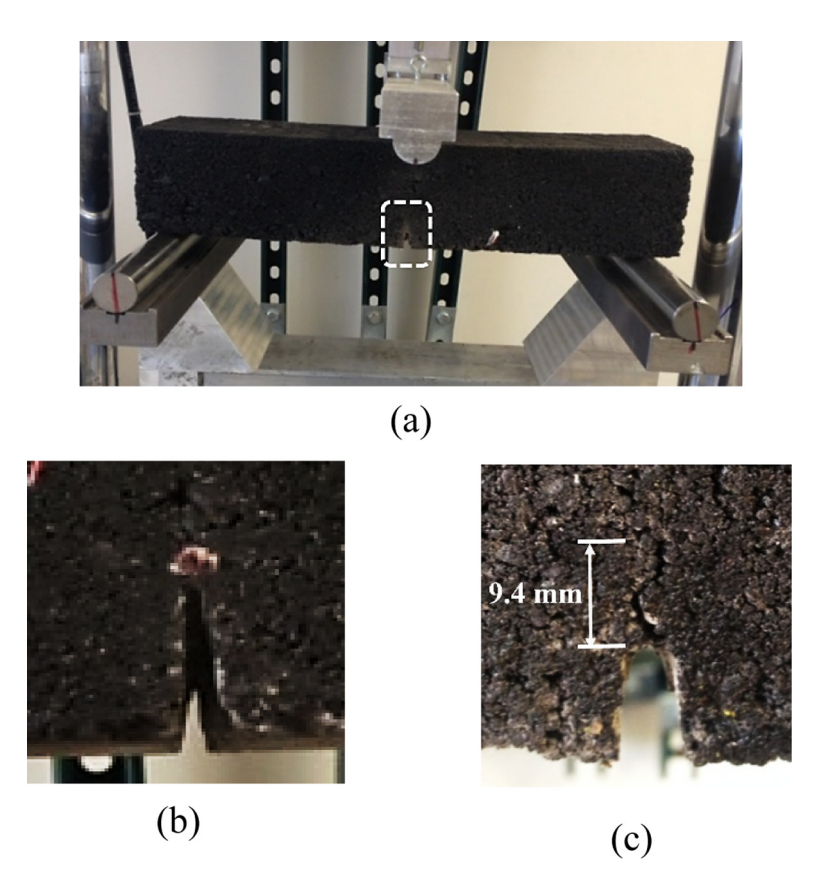


Fig. 11. (a) Three-point bending experimental setup, (b) notch at the initial stage, and (c) crack propagation phase.

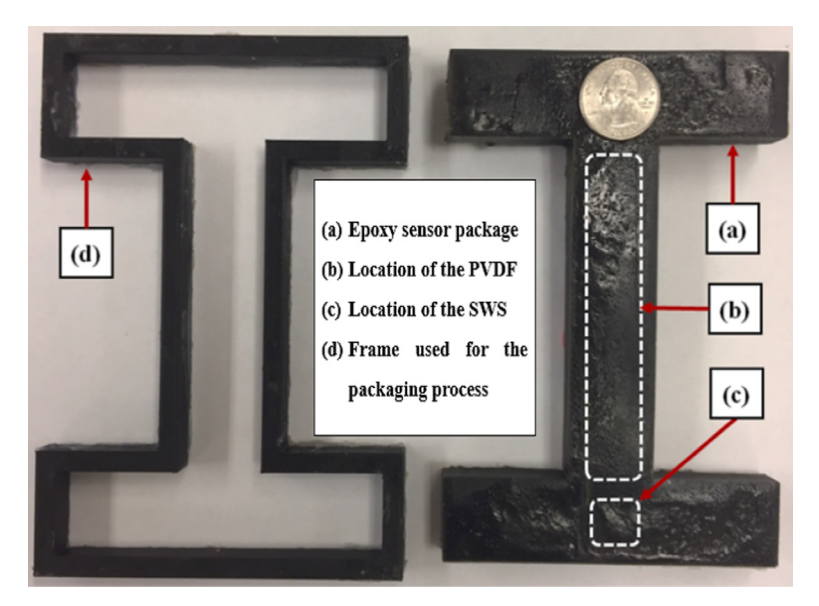


Fig. 12. Sensor packaging design to protect the PVDF and the sensor electronics.

threshold of the first five channels. Therefore, gates 1 to 5 are recording the cumulative strain droppage for all damage states, while gate 6 only recorded damage states D3 and D4. This is because the maximum strain values for damage states D0, D1 and D2 did not exceed the strain threshold level of gate 6 and therefore, this gate remained closed. As soon as the strain exceeded the activation value of this gate (for damage states D3 and D4), the gate starts recording. Gate 7 merely recorded the most severe damage state, i.e. D4. As a summary, the slope representing the sensor strain versus the number of cycles is good damage indicator. In addition, the gate number could be also used to detect severe cracks at the bottom of the pavement. In fact, gates 6 and 7 start recording only when the crack reaches high values. An interesting observation from Fig. 10 is that the increasing trend of the strain droppage percentage is a good indicator of the damage severity, particularly for the activated gates.

4. Experimental study

4.1. Test setup

The three-point bending test setup for the experimental study is shown in Fig. 11. The slab was built using hot mix asphalt (HMA), 4E1 mixture type. The weight of the HMA was 12.5 kg and the length of the slab was equal to 450 mm (17.71 in). The loading protocol consisted of applying a gradually increasing compressive force to the top mid-span of the beam using a universal mechanical testing frame. In this study, a polyvinylidene

fluoride (PVDF) piezoelectric film was used to harvest the strain energy from the host structure. In order to protect the piezoelectric film and the sensor electronics from possible damage during the manufacturing of the asphalt concrete specimen, an H-shape packaging was designed (Fig. 12). Conathane® TU-981 epoxy was used for encasing the proposed H-shape packaging system. A PVDF with a size of 7.3 cm covered by epoxy was embedded inside the asphalt layer at a distance of approximately 30 mm from the bottom of the layer. Fig. 13 displays an image of the used PVDF and its dimensions. The PVDF dimensions and properties are summarized in Table 3. Before starting the test, a preload equal to 0.5 kN was applied to the sample to ensure it is seated on the fixture.

A cyclic displacement loading similar to the FE simulations was applied to the sample. Damage was introduced by making a notch at the bottom of the asphalt specimen. The damage states were defined by increasing the notch size (a) as follows:

Table 4Voltage threshold levels of each gate.

| Gate number | Voltage (V) |
|-------------|-------------|
| 1 | 7.6 |
| 2 | 8.1 |
| 3 | 8.5 |
| 4 | 8.8 |
| 5 | 9.0 |
| 6 | 9.7 |
| 7 | 10.2 |

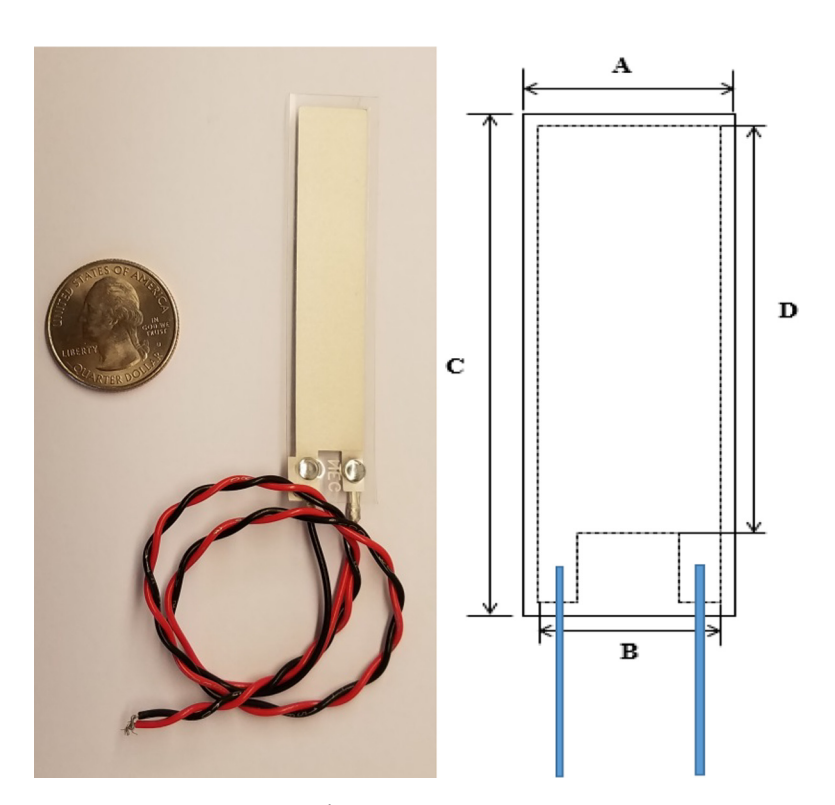


Fig. 13. LDT2-28K PVDF.

Table 3 PVDF dimensions and properties.

| PVDF type | A (mm) | B (mm) | C (mm) | D (mm) | Thickness (µm) | Capacitance (nF) |
|-----------|--------|--------|--------|--------|----------------|------------------|
| LDT2-028K | 16 | 12 | 73 | 62 | 157 | 2.85 |

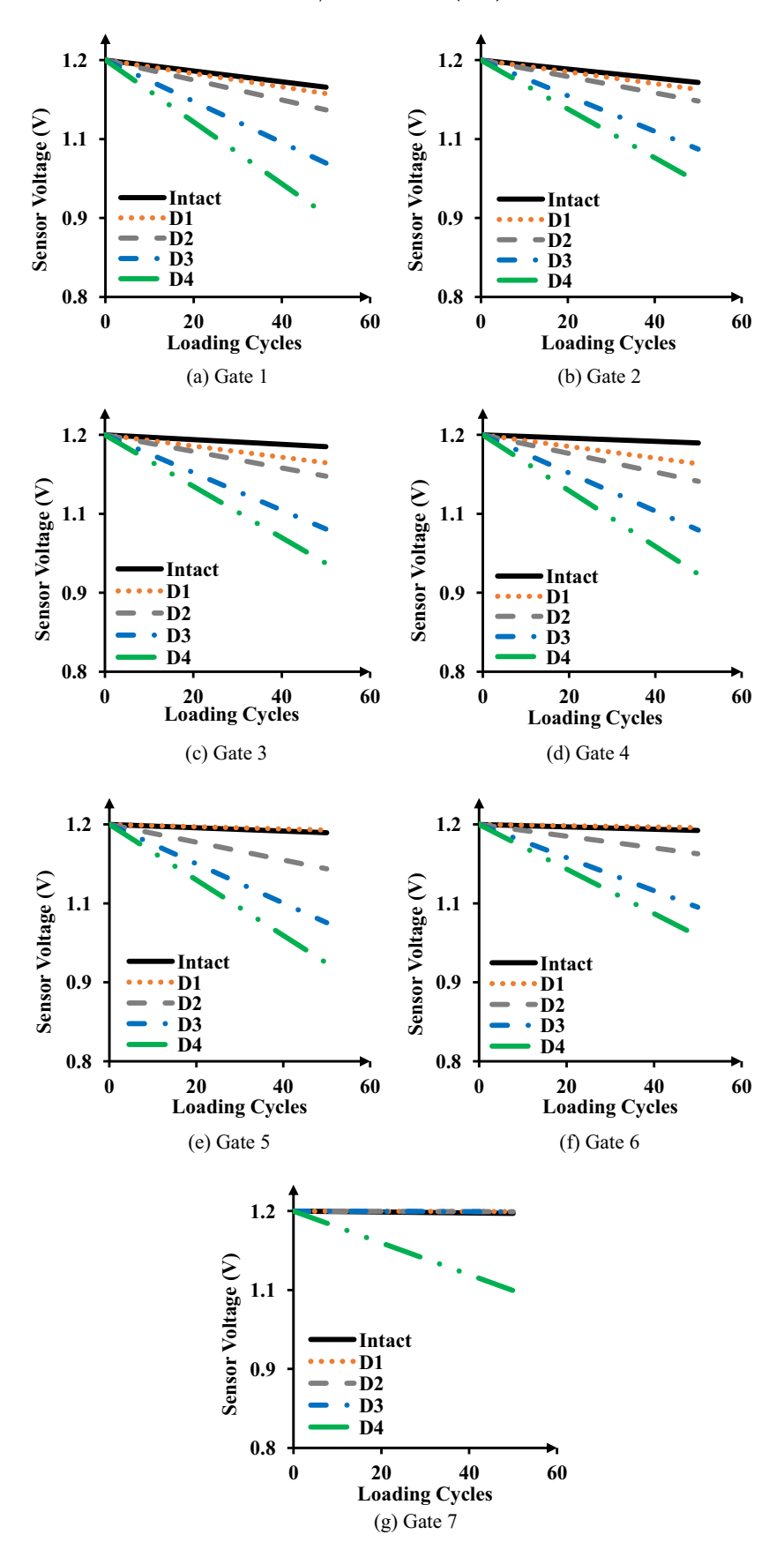
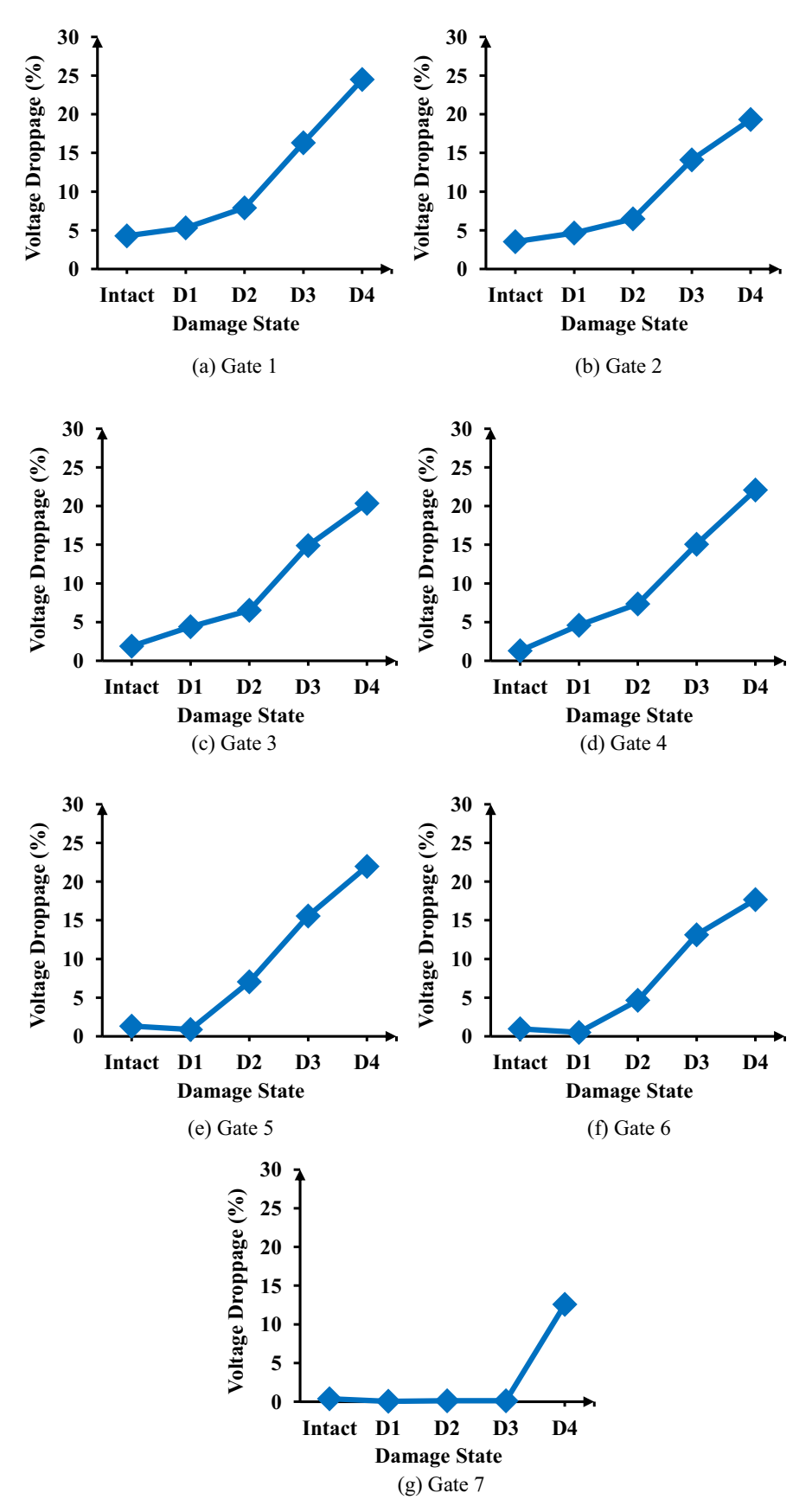


Fig. 14. Voltage changes across the floating-gates of the SWS.



 $\textbf{Fig. 15.} \ \ \text{Percentage of voltage droppage for different gates of the sensor.}$

Intact (D0): Intact plate (a = 0 mm)
Damage 1 (D1): a = 6.35 mm (1/4")
Damage 2 (D2): a = 15.875 mm (5/8")

After introducing the second damage phase, the displacement was increased to 2 mm to evaluate the behavior of the sample for higher amplitudes. After a number of cyclic loadings, a crack propagation phenomenon was observed (Fig. 11(c)). The crack propagated two times with a length of 3.2 mm and 9.4 mm. These new damage phases were considered as Damages 3 and 4. Accordingly, the total crack length for Damages 3 and 4 were, respectively, equal to 19.1 mm and 25.3 mm.

- Damage 3 (D3) (propagated crack): a = 19.1 mm
- Damage 4 (D4) (propagated crack): a = 25.3 mm

For each of the tests, the initial voltage of the gates was set to 1.2 V. Then, the voltage was read after applying 50 cycles. The initial voltage value dropped after applying the cycling loading due to electrons injection. Therefore, after each test, the sensor was tunneled and injected to reset all gates to almost the same voltage. The goal is to find a relationship between the voltage droppage and damage progression. Based on a series of preliminary tests, the voltage thresholds of gates 1 to 7 are summarized in Table 4.

4.2. Damage detection results

The voltage droppage per 50 cycles with respect to different damage states for the seven gates is presented in Fig. 14. The corresponding percentages of voltage droppage are shown in Fig. 15. As soon as the voltage generated by the PVDF exceeds a threshold corresponding to one of the gates, the procedure of electron injection initiates, and subsequently the voltage of that gate starts decreasing. It can be seen that the voltage droppage rate increases when damage progresses. This is evident for all of the 7 gates onboard the sensor, specifically for gates 1–6. Gate 7 is activated at a higher voltage threshold (>10.2 V), and therefore it started injecting after the fourth damage state.

Apparently, the gate activation can be considered as an indicator of damage occurrence. The other important observation from Fig. 15 is that the voltage droppage percentage for each gate is also a good indicator of damage progression. For instance, consider the response of gate 1 to the voltage generated by the PVDF for D0 to D4 damage states (Fig. 15(a)). Since the voltage amplitude was higher for the D4 mode than that for the other modes, the injection time was higher, and therefore the voltage on the gate dropped more for this mode. The same is true for the D3-D2, D2-D1 and D1-D0 cases. These trends are similar to those observed from the FE results.

5. Conclusions

This paper presented a new method for detecting bottom-up cracking in asphalt concrete pavements based on the data recorded by the SWS. The whole methodology is based on detecting the deviation of the voltage/strain amplitude caused by the damage or cracking events. The prototypes of the SWS can have floating-gates with constant and variable electron injection rates. The injection rate controls the injection of the electrons into the gate and therefore the voltage droppage across it. The sensor records the cumulative time at specific voltage threshold which is proportional to this droppage. Each sensor has seven memory gates for data storage and an activation threshold level from which the sensor start recording the cumulative droppage of the voltage/strain. Based on previous

studies, the output of the sensor with the constant injection rates can be characterized by a Gaussian CDF. However, analysis of the sensor output is challenging for the case of a sensor with non-constant injection rates which is the case of this study. A series of experiments and numerical simulations were conducted on an asphalt concrete specimen under three-point bending configuration to analyze the sensor performance. Based on the results, the strain amplitude changes with increasing the notch size. Consequently, the measured voltage from the PVDFs increases as well. The other important observation was that the slope (in absolute value) of the curves representing the sensor strain/voltage versus the number of applied cycles increases as damage progresses. More, the percentage of voltage/strain droppage can be considered as good indicator of damage progression, and the gate number and activation are good indicators of damage severity. Although the performance of the sensor was evaluated in an AC slab under three-point bending configuration, future research is needed to verify the efficiency of the proposed technique in real pavement structure. In addition, the obtained results are based on the experiments carried out at room temperature (25 °C). Therefore, the effect of the environmental conditions and season variability on the sensor and on the piezoelectric material should be investigated in depth.

Acknowledgement

The presented work is supported by a research grant from the Federal Highway Administration (FHWA) (DTFH61-13-C-00015).

Appendix A

See Table A1.

Table A1 Prony series coefficients.

| ğί | \bar{k}_i | τ_{i} |
|------------|-------------|------------|
| 6.6622E-05 | 6.6622E-05 | 1.00E-13 |
| 0.00012834 | 0.00012834 | 6.49E-13 |
| 0.00024903 | 0.00024903 | 4.22E-12 |
| 0.00048324 | 0.00048324 | 2.74E-11 |
| 0.00093704 | 0.00093704 | 1.78E-10 |
| 0.00181707 | 0.00181707 | 1.15E-09 |
| 0.00351793 | 0.00351793 | 7.50E-09 |
| 0.00680272 | 0.00680272 | 4.87E-08 |
| 0.01309445 | 0.01309445 | 3.16E-07 |
| 0.02504117 | 0.02504117 | 2.05E-06 |
| 0.04711772 | 0.04711772 | 1.33E-05 |
| 0.08602016 | 0.08602016 | 8.66E-05 |
| 0.14652054 | 0.14652054 | 0.000562 |
| 0.21559013 | 0.21559013 | 0.003652 |
| 0.23267158 | 0.23267158 | 0.023714 |
| 0.1499758 | 0.1499758 | 0.153993 |
| 0.0529047 | 0.0529047 | 1 |
| 0.01273171 | 0.01273171 | 6.493816 |
| 0.00289254 | 0.00289254 | 42.16965 |
| 0.00077742 | 0.00077742 | 273.842 |
| 0.00025633 | 0.00025633 | 1778.279 |
| 0.0001018 | 0.0001018 | 11547.82 |
| 4.4828E-05 | 4.4828E-05 | 74989.42 |
| 2.1436E-05 | 2.1436E-05 | 486967.5 |
| 1.0515E-05 | 1.0515E-05 | 3162278 |
| 5.3281E-06 | 5.3281E-06 | 20535250 |
| 2.6994E-06 | 2.6994E-06 | 1.33E+08 |
| 1.3899E-06 | 1.3899E-06 | 8.66E+08 |
| 7.0905E-07 | 7.0905E-07 | 5.62E+09 |
| 3.7066E-07 | 3.7066E-07 | 3.65E+10 |
| 1.8002E-07 | 1.8002E-07 | 2.37E+11 |
| 1.1627E-07 | 1.1627E-07 | 1.54E+12 |
| 2.2759E-08 | 2.2759E-08 | 1E+13 |
| | | |

References

- W. Xue, L. Wang, D. Wang, C. Druta, Pavement health monitoring system based on an embedded sensing network, J. Mater. Civ. Eng. 26 (10) (2014) 04014072.
- [2] J.F. Potter, H.C. Mayhew, A.P. Mayo, Instrumentation of the Full Scale Experiment on A1 Trunk Road at Conington Huntingdonshire, Transport Research Laboratory (Road Research Laboratory), Wokingham Berkshire, U.K., 1969
- [3] A. Badr, A.G. Karlaftis, Using the asphalt pavement dynamic stiffness modulus in assessing falling weight deflectometer test results, Adv. Mater. Res. 685 (2013) 233–239.
- [4] A. Badr, A.G. Karlaftis, Duration model estimation for pavement rehabilitation and service life, Adv. Appl. Stat. 31 (1) (2012) 1–19.
- [5] A.G. Karlaftis, A. Badr, Predicting asphalt pavement crack initiation following rehabilitation treatments, Transp. Res. C 55 (2015) 510–517.
- [6] R. Huff, C. Berthelot, B. Daku, Continuous primary dynamic pavement response system using piezoelectric axle sensors, Can. J. Civ. Eng. 32 (1) (2005) 260–269.
- [7] M. Malekzadeh, G. Atia, F.N. Catbas, A hybrid data interpretation framework for automated performance monitoring of infrastructure, in: Structures Congress 2015, 2015.
- [8] M. Arraigada, M.N. Partl, S.M. Angelone, F. Martinez, Evaluation of accelerometers to determine pavement deflections under traffic loads, Mater. Struct. 42 (6) (2009) 779.
- [9] T. Ryynänen, T. Pellinen, J. Belt, The use of accelerometers in the pavement performance monitoring and analysis, in: IOP Conference Series: Mater. Sci. Eng. vol. 10, no. 1, IOP Publishing, 2010, pp. 012110.
- [10] Y. Ni, X. Lu, W. Lu, Operational modal analysis of a high-rise multi-function building with dampers by a Bayesian approach, Mech. Syst. Sig. Process. 86 (2017) 286–307.
- [11] M.H. Mohajeri, P.J. Manning, ARIA: An Operating System of Pavement Distress Diagnosis by Image Processing, Transportation Research Record 1311, Transportation Research Board, Washington, DC, 1991, pp. 120–130.
- [12] H. Koutsopoulos, A. Downey, Primitive based classification of pavement cracking images, J. Transp. Eng. 119 (3) (1993) 402–418.
- [13] J.P. Mills, I. Newton, G.C. Peirson, Pavement deformation monitoring in a rolling load facility, Photogramm. Rec. 17 (97) (2001) 7–24.
- [14] C.P. Plati, A. Loizos, Estimation of in-situ density and moisture content in HMA pavements based on GPR trace reflection amplitude using different frequencies, J. Appl. Geophys. 97 (2013) 3–10.
- [15] C. Plati, P. Georgiou, A. Loizos, Use of infrared thermography for assessing HMA paving and compaction, Transp. Res. C 46 (2014) 192–208.
- [16] M. Bagherifaez, A. Behnia, A. Majeed, H.K. Chai, Acoustic emission monitoring of multi-cell reinforced concrete box girders subjected to torsion, Sci. World J. (2014).
- [17] A. Behnia, H.K. Chai, M. Yorikawa, S. Momoki, M. Terazawa, T. Shiotani, Integrated non-destructive assessment of concrete structures under flexure by acoustic emission and travel time tomography, Constr. Build. Mater. 67 (Part B) (2014) 202–215.
- [18] D. Xu, S. Banerjee, Y. Wang, S. Huang, X. Cheng, Temperature and loading effects of embedded smart piezoelectric sensor for health monitoring of concrete structures, Constr. Build. Mater. 76 (2015) 187–193.
- [19] B.A. Sundaram, K. Ravisankar, R. Senthil, S. Parivalla, Wireless sensors for structural health monitoring and damage detection techniques, Curr. Sci. 104 (11) (2013) 1496–1505.
- [20] D.G. Watters, P. Jayaweera, A.J. Bahr, D.L. Huestis, N. Priyantha, R. Meline, R. Reis, D. Parks, Smart pebble: wireless sensors for structural health monitoring of bridge decks, Proc. SPIE 5057 (2003) 20–28.

- [21] J.P. Lynch, K.J. Loh, A summary review of wireless sensors and sensor networks for structural health monitoring, Shock Vib. Digest 38 (2006) 91–128.
- [22] S. Ukkusuri, L. Du, Geometric connectivity of vehicular ad hoc networks: analytical characterization, Transp. Res. C 16 (5) (2008) 615–634.
- [23] H. Salehi, T. Taghikhany, A.Y. Fallah, Seismic protection of vulnerable equipment with semi-active control by employing robust and clippedoptimal algorithms, Int. J. Civ. Eng. 12 (4) (2014) 413–428.
- [24] G. Park, T. Rosing, M.D. Todd, C.R. Farrar, W. Hodgkiss, Energy harvesting for structural health monitoring sensor networks, J. Infrastruct. Syst. 14 (1) (2008) 64–79.
- [25] N. Lajnef, R. Burgueño, W. Borchani, Y. Sun, A. Heeringa, Characterization of mechanically-equivalent amplifiers and frequency modulating concepts for energy harvesting devices, in: ASME Conference on Smart Materials, Adaptive Structures and Intelligent Systems, Stone Mountain, GA, September 2012.
- [26] N. Lajnef, W. Borchani, R. Burgueño, S. Chakrabartty, Self-powered Piezo-Floating-Gate smart-gauges based on quasi-static mechanical energy concentrators and triggers, IEEE Sens. J. 15 (2) (2015) 676–683.
- [27] A. Aladwani, O. Aldraihem, A. Baz, Piezoelectric vibration energy harvesting from a two-dimensional coupled acoustic-structure system with a dynamic magnifier, J. Vib. Acoust. 137 (3) (2015) 031002.
- [28] S. Roundy, P.K. Wright, J. Rabaey, A study of low level vibrations as a power source for wireless sensor nodes, Comput. Commun. 26 (2002) 1131–1144.
- [29] N. Lajnef, S. Chakrabartty, N. Elvin, A piezo-powered floating-gate sensor array for long-term fatigue monitoring in biomechanical implants, IEEE Trans. Biomed. Circuits Syst. 2 (3) (2008) 164–172.
- [30] I. Korhonen, R. Lankinen, Energy harvester for a wireless sensor in a boiler environment, Meas. 58 (2014) 241–248.
- [31] P. Jiao, B. McGraw, A. Chen, J.F. Davalos, I. Ray, Flexural-torsional buckling of cantilever composite wood I-beams with sinusoidal web geometry, Earth and Space (2012) 684–693, http://dx.doi.org/10.1061/9780784412190.074.
- [32] A. Chen, J.F. Davalos, P. Jiao, B. McGraw, Buckling behavior of sinusoidal web for composite wood I-joist with elastically restrained loaded edges under compression, J. Eng. Mech. 139 (2013) 1065–1072.
- [33] W. Borchani, N. Lajnef, R. Burgueño, Model development for Dynamic Energy Conversion in post-buckled multi-stable slender columns, in: ASME Conference on Smart Materials, Adaptive Structures and Intelligent Systems, Newport, Rhode Island, September 2014.
- [34] N. Elvin, A. Elvin, M. Spector, A self-powered mechanical strain energy sensor, Smart Mater. Struct. 10 (2001) 293–299.
- [35] N. Lajnef, K. Chatti, S. Chakrabartty, M. Rhimi, P. Sarkar, Smart Pavement Monitoring System, Report: FHWA-HRT-12-072, Federal Highway Administration (FHWA), Washington, DC, 2013.
- [36] H. Salehi, S. Das, S. Chakrabartty, S. Biswas, R. Burgueno, Structural Assessment and Damage Identification Algorithms Using Binary Data, in: ASME 2015 Conference on Smart Materials, Adaptive Structures and Intelligent Systems (SMASIS2015), Colorado Springs, Colorado, 2015.
- [37] A.H. Alavi, H. Hasni, N. Lajnef, K. Chatti, F. Faridazar, An intelligent structural damage detection approach based on self-powered wireless sensor data, Autom. Constr. 62 (2016) 24–44.
- [38] A.H. Alavi, H. Hasni, N. Lajnef, K. Chatti, Continuous health monitoring of pavement systems using smart sensing technology, Constr. Build. Mater. 114 (2016) 719–736.
- [39] A.H. Alavi, H. Hasni, N. Lajnef, K. Chatti, Damage growth detection in steel plates: Numerical and experimental studies, Eng. Struct. 128 (2016) 124–138.
- [40] H. Hasni, A.H. Alavi, P. Jiao, N. Lajnef, Detection of fatigue cracking in steel bridge girders: a support vector machine approach, Arch. Civil Mech. Eng. 17 (3) (2017) 609–622.